The Development of a Long-Stroke Precision Positioning Stage for Micro Fabrication by Two-Photon Polymerization

Fu-Cheng Wang*, Yi-Yi Chen*, Kuo-An Wang* and Tien-Tung Chung*

* *Department of Mechanical Engineering, National Taiwan University, Taipei, Taiwan*
No. 1, Roosevelt Road, Sec. 4, Taipei 10617, Taiwan
Email : fcw@ntu.edu.tw

This paper applies a combined precision stage to fabricate micro-structures by two-photon polymerization (TPP). The combined stage consists of PZT and stepper-motor stages to achieve precision positioning in long displacements. First, we derive the models of the stages by identification experiments. Second, we apply robust loop-shaping techniques to improve the positioning performance of the stages. Third, we integrate the stages and develop a multi-loop control structure to provide long-stroke and high precision. In addition, we propose coordinate transformation and anti-locking functions for further improvement of the system performance. Last, we apply the combined stage to a TPP system for fabricating micro-structures, and define performance indexes based on image processing and optical qualities. The obtained performance criteria can be used to adjust controller design to improve precision manufacturing.

DOI: 10.2961/jlmn.2016.01.0001
Keywords: two-photon polymerization; micro manufacturing; piezoelectric actuator; combined stage; precision positioning; robust control; loop-shaping.

1. Introduction

Precision positioning is increasingly important as technologies advance. Piezoelectric transducer (PZT) materials are commonly applied in precision control because of their fast responses and high resolution. However, PZT nonlinearities, such as hysteresis and creep, have the potential to cause problems in precision positioning and could degrade system performance. Therefore, researchers have applied advanced control to PZT systems. For example, Xu [1] designed digital sliding mode (DSM) prediction control to drive a PZT stage and achieved higher bandwidth and better precision than is obtainable with traditional proportional integral derivative (PID) control. Peng et al. [2] applied a PID-based sliding mode observer to eliminate the nonlinear hysteresis and creep, and achieved a tracking frequency of 150Hz with sub-micro precision. Kenton et al. [3] used model-based feedforward control for adaptive tracking of various frequencies of AFM images. Yi et al. [4] applied state estimators to eliminate PZT hysteresis, and designed a PID controller to track 100Hz sinusoidal signals with nano precision. Liu et al. [5] divided the hysteresis model into linear and nonlinear parts, and achieved a tracking error of 5% for 600Hz signals with inversed model control. Because the PZT displacements are limited, some research has integrated PZT with other mechanisms to enlarge the working ranges. For instance, Wu et al. [6] integrated a bi-axial stepper-motor stage and a tri-axial PZT stage to accomplish multi-axial strokes of 100 mm. On the other hand, some mechanisms are proposed to increase the moving range of the PZT; for example, Li et al [7] designed inch-worm mechanisms that allowed PZT movement within 11mm with a resolution of 10 nm.

We have developed the long-stroke nano-positioning stage in previous studies [6][8]. The combined stage has achieved a travel of 1mm with a root-mean-square error (RMSE) of 4.2nm [6], but with misalignment error. Therefore, we proposed the control structure to compensate the misalignment error and achieved a travel of 500μm [8]. This paper proposes a tri-axial long-stroke precision positioning stage, which integrates a tri-axial PZT stage and a bi-axial stepper-motor stage. We apply robust loop-shaping control to the combined stage to achieve a travel of 10cm with nano-precision. Furthermore, we integrate the stage with a two-photon polymerization (TPP) system to fabricate micro-structures. TPP was developed based on Two-Photon Absorption (TPA) [9][10], where a molecule of material simultaneously absorbs two photons from a focused laser beam and is excited from the ground state to a higher state [11][12]. Compared with one-photon absorption (OPA), TPA requires higher reaction conditions and achieves higher fabricating resolution; thus, it has become a popular method for fabricating high quality micro-structures. For example, Kumpfmueller et al. [13] proposed two-photon-induced microfabrication of flexible optical waveguides. Stitichel et al. [14] applied TPP to construct large scale biomedical scaffolds. Do et al. [15] discussed a new 3D fabrication method to make micro-structures by commercial SU8 photoresist, using a continuous-wave laser of 532 nm with several milli-watts. Wu et al. [16] presented three phase-type fractal zone plates fabricated by femtosecond laser. They then developed in-channel integration of flexible micro-optical by flat scaffold-supported hybrid femtosecond laser microfabrication (FSS-HFLM) [17]. In this paper, we used an Nd:YAG laser to trigger the

TPP of resin to make micro-structures. We examined the fabricated micro-structures with a microscope, and defined performance indexes by image processing and imaging quality analysis. Based on the results, we can further adjust the controller design procedures to improve the system performance.

This paper is organized as follows: Section 2 describes the PZT and the stepper-motor stages and derives their dynamic models by experiments; Section 3 applies loop-shaping techniques to design robust controllers for the stages; Section 4 combines the stages to achieve long-stroke nano-positioning, and designs a multi-loop control structure with coordinate transformation and anti-locking functions to improve system performance. Section 5 integrates the combined stage with a TPP system to fabricate micro-structures, including words, gratings, and micro-lenses. In addition, we define performance indexes and adjust the designed controllers accordingly to improve fabrication qualities. Last, we draw conclusions in Section 6.

2. System description and identification

The combined stage is shown in Fig. 1(a); it consists of a 2D PZT stage, a z-axis PZT, and a stepper-motor stage. The 2D PZTs control displacements on the x-y axes, and are equipped with encoders of 1.2nm resolution. The z-axis displacement is driven by a PZT with a linear variable differential transformer (LVDT), to achieve a resolution of 0.01% of the full displacement. The stepper-motor stage was equipped with two stepper motors to provide 100mm × 100mm displacements on the x-y axes, with encoders of 0.1μm resolution. The hardware specifications are illustrated in Table 1. We integrated the PZT and stepper-motor stages to accomplish precision positioning over long travel ranges.

The measurement and control layouts of the combined stage are illustrated in Fig. 1(b). For the PZT stages, we fed back the displacement signals by data-acquisition (DAQ) boards DAQ PCI-6221, PCI-6229, and PCI-6220. In addition, we used DAQ PCI-6229 to transmit the control signals and amplified them ten-fold using an E-663 amplifier and SVR. On the other hand, for the stepper-motor stage, we fed back the encoder signals by DAQ PCI-6220, and used PCI-6221 and PCI-6229 to control the stepper-motors by pulse-width modulation signals.

Table 1 Instrument specifications

The PZT stage	
Active axes	x, y, z
Sensor resolution	1.22nm/0.01% output
Travel	15μm, 15μm /80μm
Voltage range	-20V to 120V
The stepper-motor stage	
Active axes	x, y
Sensor resolution	0.1μm
Travel	100mm
Maximum speed	8mm/s

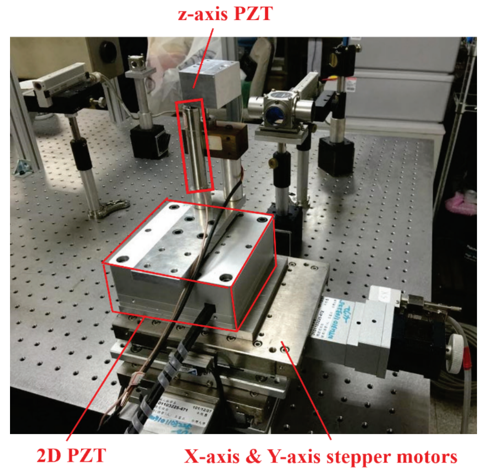

(a) The combined stage

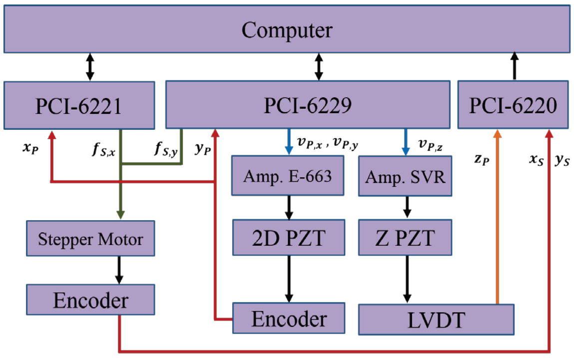

(b) The hardware layouts

Fig. 1 The long-stroke precision positioning stage.

2.1 Identification of PZT stage

The PZT models were derived by identification experiments. First, we applied a swept sinusoidal signal, $v_{P,x} = v_{P,y}$, with a frequency range of 0.001–200 Hz and a magnitude of 7V, to drive the 2D PZT. For the *z*-axis PZT, we applied a swept sinusoidal signal $v_{P,z}$ with a frequency range of 0.001–100 Hz and a magnitude of 8V. Second, we measured the corresponding PZT displacements x_P and y_p by the encoders and z_P by the LVDT. The input and output signals of the y-axis are shown in Fig. 2(a), while the x- and y-axis signals are similar. Last, we applied the numerical subspace state space system identification (N4SID) methods [18] to derive the PZT models. Considering the system variation, we repeated the experiments ten times for each axis, and defined the transfer functions as:

$$G_P^{x_i}(s) = T_{v_{P,x}\to x_P}(s),\ G_P^{y_i}(s) = T_{v_{P,y}\to y_P}(s),\ G_P^{z_i}(s) = T_{v_{P,z}\to z_P}(s) \quad (1)$$

for $i = 1, 2, \cdots, 10$. The Bode plots of $G_P^{y_i}(s)$ are shown in Fig. 2(b) for demonstration, while $G_P^{x_i}(s)$ and $G_P^{z_i}(s)$ are derived in a similar way.

2.2 Identification of the stepper-motor stage

Similarly, for the stepper stage, we applied a swept sinusoidal input signal ($f_{S,x} = f_{S,y}$) with a frequency range of 0.001–20 Hz and a magnitude of ±20,000 pulses per second to make the motors move within a velocity of ±2 mm/s, and we recorded the corresponding displacements x_S and y_S of the encoders, as shown in Fig. 2(c). We took system variation into account by repeating the identification five times for each axis and we applied the N4SID method to derive the following transfer functions:

$$G_S^{x_i}(s) = T_{f_{S,x} \to x_S}(s),\ G_S^{y_i}(s) = T_{f_{S,y} \to y_S}(s) \qquad (2)$$

for $i = 1,\ 2, \cdots,\ 5$, with the Bode plots shown in Fig. 2(d). These transfer functions were then used for controller design and simulations in the next sections.

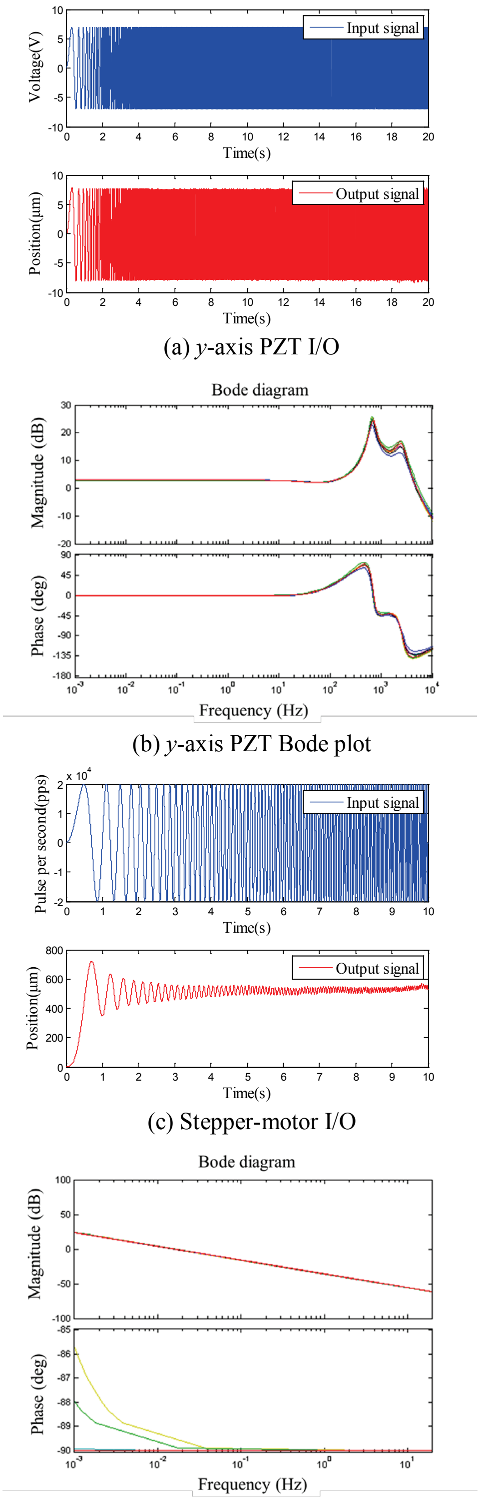

(a) y-axis PZT I/O

(b) y-axis PZT Bode plot

(c) Stepper-motor I/O

(d) Stepper-motor Bode plot

Fig. 2 Identification of the PZT and stepper-motor stages.

3. Controller design

This section designs robust controllers for the PZT and stepper-motor stages. We chose the nominal plants from the identified models by gap metric analysis, and then applied loop-shaping techniques to improve system performance.

3.1 Controller design for the PZT stage

Note in Fig. 2(b) that the PZT models varied for each experiment. Therefore, we can regard the system as linear transfer functions with uncertainties and disturbances, and apply robust control techniques to guarantee system stability and to improve system performance. Suppose a nominal plant G_N has the following normalized left coprime factorization:

$$G_N = \tilde{M}^{-1}\tilde{N} \qquad (3)$$

where $\tilde{M}, \tilde{N} \in RH_\infty$ and $\tilde{M}\tilde{M}^* + \tilde{N}\tilde{N}^* = I$. Assume the perturbed plant G_Δ can be represented as $G_\Delta = (\tilde{M} + \Delta_{\tilde{M}})^{-1}(\tilde{N} + \Delta_{\tilde{N}})$ with $\Delta_{\tilde{M}}, \Delta_{\tilde{N}} \in RH_\infty$. Because coprime factorization of a system is not unique, we can define the *gap* between the nominal plant G_N and the perturbed plant G_Δ as [19]: *The smallest value of* $\left\| \begin{bmatrix} \Delta_{\tilde{N}} & \Delta_{\tilde{M}} \end{bmatrix} \right\|_\infty < \varepsilon$ *which perturbs* G_N *into* G_Δ *is called the gap between* G_N *and* G_Δ, *denoted as* $\delta(G_N, G_\Delta)$. The gap $\delta(G_N, G_\Delta) \in [0 \quad 1]$ indicates the difference between the two plants. Therefore, we can select a nominal plant G_N from the models that minimizes the maximum gaps between G_N and the other plants, as follows:

$$G_N = \arg\left\{ \min_{G_N} \max_{G_i} \delta(G_N, G_i) \right\}, \forall G_i \qquad (4)$$

Based on (2), we selected the following nominal plants for the PZT stage:

$$\begin{aligned} G_{N,P}^x &= G_P^{x_4} = \\ &\frac{6.553\times10^5 s^4 + 6.731\times10^8 s^3 + 3.664\times10^{12} s^2 + 2.095\times10^{15} s + 2.649\times10^{17}}{s^5 + 996.4s^4 + 7.609\times10^7 s^3 + 3.037\times10^{10} s^2 + 1.151\times10^{15} s + 1.935\times10^{17}}, \\ G_{N,P}^y &= G_P^{y_5} = \\ &\frac{1.540\times10^4 s^4 + 6.754\times10^8 s^3 + 4.383\times10^{12} s^2 + 6.484\times10^{15} s + 1.201\times10^{18}}{s^5 + 9098s^4 + 2.899\times10^8 s^3 + 4.700\times10^{11} s^2 + 4.738\times10^{15} s + 8.599\times10^{17}} \\ G_{N,P}^z &= G_P^{z_6} = \\ &\frac{157.1s^4 + 9.653\times10^4 s^3 + 7.005\times10^7 s^2 + 3.434\times10^{10} s + 3.121\times10^{11}}{s^5 + 716.7s^4 + 5.071\times10^5 s^3 + 2.33\times10^8 s^2 + 1.370\times10^{10} s + 2.896\times10^{10}} \end{aligned} \qquad (5)$$

which gives $\delta(G_{N,P}^x, G_P^{x_i}) \le 0.157$, $\delta(G_{N,P}^y, G_P^{y_i}) \le 0.094$, and $\delta(G_{N,P}^z, G_P^{z_i}) \le 0.096$ for the x-, y-, and z-axis, respectively. These gaps can be regarded as the maximum system variations due to system uncertainties and operating conditions.

A closed-loop system with a perturbed plant G_Δ and a controller K can be represented as ([6], Fig. 5(a)), and rearranged as ([6], Fig. 5(b)). Therefore, from the Small Gain Theorem [20][21], the system is internally stable for all perturbations with $\left\| \begin{bmatrix} \Delta_{\tilde{N}} & \Delta_{\tilde{M}} \end{bmatrix} \right\|_\infty \le \varepsilon$, if and only if

$$\left\| \begin{bmatrix} K \\ I \end{bmatrix} (I - G_N K)^{-1} \tilde{M}^{-1} \right\|_\infty = \left\| \begin{bmatrix} K \\ I \end{bmatrix} (I - G_N K)^{-1} \begin{bmatrix} I & G_N \end{bmatrix} \right\|_\infty < \frac{1}{\varepsilon} \tag{6}$$

Hence, we can further define the system's stability margin $b(G_N, K)$ as:

$$b(G_N, K) = \left\| \begin{bmatrix} K \\ I \end{bmatrix} (I - G_N K)^{-1} \begin{bmatrix} I & G_N \end{bmatrix} \right\|_\infty^{-1} \tag{7}$$

so that the closed-loop system is internally stable for all uncertainties with $\left\| \begin{bmatrix} \Delta_{\tilde{N}} & \Delta_{\tilde{M}} \end{bmatrix} \right\|_\infty \le \varepsilon$, if and only if its stability margin $b(G_N, K) > \varepsilon$. Thus, the goal of robust control can be represented as in Fig. 3: design a controller K for the nominal plant G_N such that $b(G_N, K)$ is greater than the system gaps.

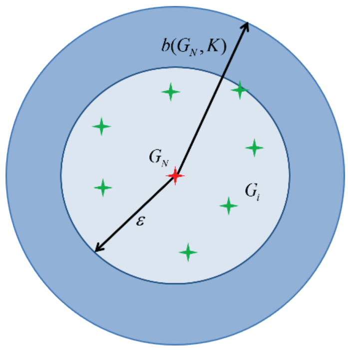

Fig. 3 The philosophy of robust control.

We further applied H_∞ loop-shaping techniques [22][23] to improve system performance. The principles are to increase system gains at the low frequency ranges to suppress system disturbances, and to decrease system gains at the high frequency ranges to attenuate system noises. We iteratively adjusted the weighting functions and verified by experiments, and selected the following weighting function for the PZT stage:

$$W_P^x = \frac{572(s + 2\pi \times 50)}{s(s + 2\pi \times 60)}, \quad W_P^y = \frac{600(s + 2\pi \times 50)}{s(s + 2\pi \times 60)}, \quad W_P^z = \frac{500(s + 2\pi \times 10)}{s(s + 2\pi \times 100)} \tag{8}$$

The bode plots of the y-axial nominal and weighted plants are shown in Fig. 4(a), where the gains were increased at the low frequency ranges. Note that the x- and z-axial bode plots are shaped in a similar way. Using these weighting functions (4), we designed the following K_∞ controllers:

$$\begin{aligned} K_\infty^x &= \frac{2.221s^4 + 1.714\times10^4 s^3 + 6.086\times10^7 s^2 + 3.350\times10^{10} s + 3.665\times10^{13}}{s^4 + 4.568\times10^4 s^3 + 3.971\times10^7 s^2 + 2.246\times10^{11} s + 8.081\times10^{13}}, \\ K_\infty^y &= \frac{0.9502s^4 + 7323s^3 + 2.531\times10^8 s^2 + 6.810\times10^{10} s + 1.911\times10^{15}}{s^4 + 1.463\times10^4 s^3 + 3.247\times10^8 s^2 + 1.114\times10^{12} s + 1.826\times10^{15}}, \\ K_\infty^z &= \frac{1.237s^4 + 944.2s^3 + 5.953\times10^5 s^2 + 3.035\times10^8 s + 1.624\times10^9}{s^4 + 986s^3 + 5.146\times10^5 s^2 + 3.448\times10^8 s + 2.027\times10^9} \end{aligned} \tag{9}$$

which gave the stability margins of $b(W_P^x G_{N,P}^x, K_\infty^x) = 0.391$, $b(W_P^y G_{N,P}^y, K_\infty^y) = 0.717$, and $b(W_P^z G_{N,P}^z, K_\infty^z) = 0.625$. These stability margins are much greater than the system gaps (0.157, 0.094, and 0.096 for the x-, y-, and z-axis, respectively), thereby assuring system stability during operations. The Bode plots of the PZT controller and the plant are shown in Fig. 4(b) for demonstration, while the x- and y-axial PZT controllers are derived by the same method.

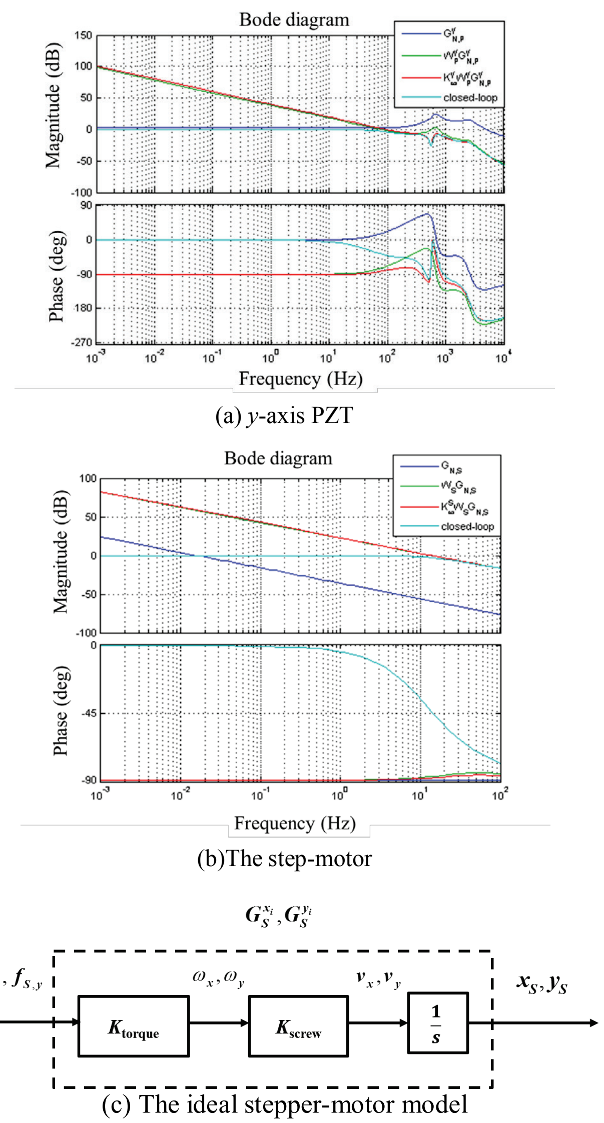

(a) y-axis PZT

(b)The step-motor

(c) The ideal stepper-motor model

Fig. 4 Robust loop-shaping control design for the stages.

3.2 Controller design for stepper-motor stage

For the stepper stage, note from Fig. 2(d) that the identified model is close to an integral 1/s. Therefore, we considered the ideal motor model of Fig. 4(c), where $K_{torque} = 1/20000$ (rps/pps) and $K_{screw} = 2$(mm/rev), and represented the mathematical model of the stepper stage, as follows:

$$G_{S,\text{ideal}}(s) = T_{f_S \to x_S} = T_{f_S \to y_S} = \frac{K_{torque} \times K_{screw}}{s} = \frac{0.1}{s} (\mu\text{m/pps}) \tag{10}$$

The gaps between $G_{S,\text{ ideal}}$ and the identified models, $G_S^{x_i}$ and $G_S^{y_i}$ are calculated as $\delta\left(G_{S,\text{ ideal}}, G_S^{x_i} \cap G_S^{y_i}\right) \le 0.008$ for $i = 1, 2, \cdots, 5$. Because the gap 0.008 is small, we can choose the ideal model of (6) as the nominal plant $G_{N,S}$ to simplify the robust control design for both axes, with an objective of finding a controller whose stability margin is greater than 0.008.

Applying the loop-shaping design, we adjusted the weighting functions by experiments and selected the following weighting function:

$$W_S = \frac{300(s+2\pi\times 60)}{(s+2\pi\times 100)} \tag{11}$$

to increase the system gain at the low-frequency range to suppress disturbances. Using the weighting function (7), we designed the following K_∞ controller:

$$K_\infty^S = \frac{0.9821s + 616.7}{s + 605.6} \tag{12}$$

which gave a stability margin of $b(W_S G_{N,S}, K_\infty^S) = 0.7135$. The stability margin is much greater than the system gap 0.008, so system stability can be assured during operations. The Bode plots of the original and weighted plants are shown in Fig. 4(b). In addition, we considered the practical velocity limitation of the stepper motor (8mm/s; see Table 1) and applied the saturation function to avoid motor stall. That is, the control signals ($f_{S,x}$ and $f_{S,y}$) should be less than or equal to 80000pps.

4. Stage integration

We integrated the PZT and the stepper-motor stage, as shown in Fig.1 (a), to achieve precision positioning for long travels. The control block diagram is shown in Fig. 5, where we shaped the command $r_{x,y,z}$ by a coordinate transformation function to compensate for the rotation angle and to correct the tilting effect.

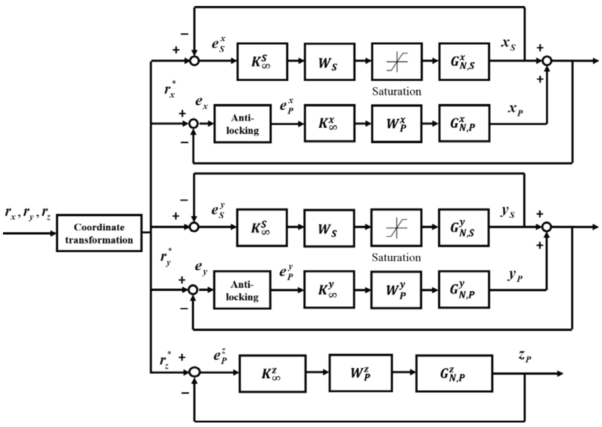

Fig. 5 The control block diagram.

4.1 Coordinate transformation

First, the rotating effect is illustrated in Fig. 6(a), where the ideal coordinate (X_{r*}, Y_{r*}) and actual coordinate (X_r, Y_r) might be misaligned and cause TPP fabrication in incorrect directions. Suppose the rotation angle is θ: the rotating effect can be compensated by the following input shaping:

$$\begin{bmatrix} r_x^* \\ r_y^* \\ r_z^* \end{bmatrix} = \begin{bmatrix} \cos\theta & -\sin\theta & 0 \\ \sin\theta & \cos\theta & 0 \\ 0 & 0 & 1 \end{bmatrix} \begin{bmatrix} r_x \\ r_y \\ r_z \end{bmatrix} \tag{13}$$

where r_i is the original command and r_i^* is the shaped command, $i = x, y, z$. The rotating angle θ can be estimated by a test-run from point A and B, as follows:

$$\theta = \tan^{-1}\frac{-y_r}{x_r} \tag{14}$$

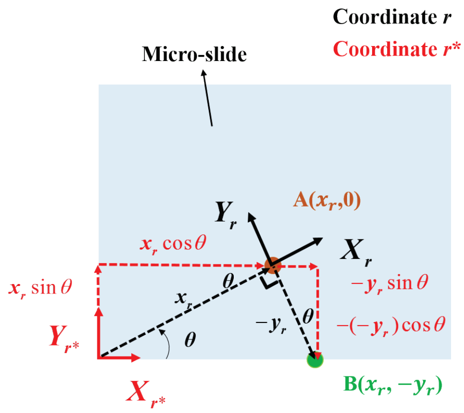

(a) The rotating effect

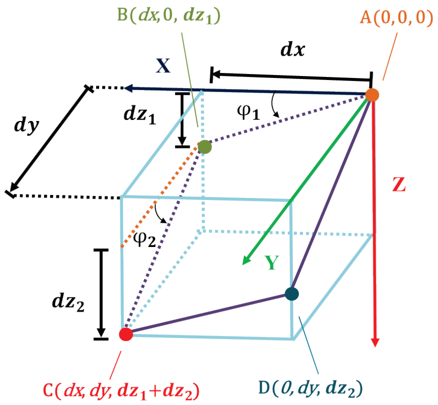

(b) The tilting effect

Fig. 6 Coordinate transformation.

Second, the tilting effect means that the stage moves with “tilting angles” and is not perpendicular to the laser, so that the laser energy cannot be correctly focused on the desired position. Consider Fig. 6(b): suppose the laser beam is in the Z-direction, while the stage moves on the ABC-plane with tilting angles of φ_1 and φ_2. Therefore, we can calculate the tilting angles φ_1 and φ_2 by conducting a test run from A to B and then B to C, as follows:

$$\varphi_1 = \tan^{-1}\frac{dz_1}{dx},\quad \varphi_2 = \tan^{-1}\frac{dz_2}{dy} \tag{15}$$

Therefore, the tilting effects can be corrected by the following transformation:

$$\begin{bmatrix} r_x^* \\ r_y^* \\ r_z^* \end{bmatrix} = \begin{bmatrix} 1 & 0 & 0 \\ 0 & 1 & 0 \\ -\tan\varphi_1 & -\tan\varphi_2 & 1 \end{bmatrix} \begin{bmatrix} r_x \\ r_y \\ r_z \end{bmatrix} \tag{16}$$

Combining (9) and (12), the overall coordinate transformation function can be derived as follows:

$$\begin{bmatrix} r_x^* \\ r_y^* \\ r_z^* \end{bmatrix} = \begin{bmatrix} \cos\theta & -\sin\theta & 0 \\ \sin\theta & \cos\theta & 0 \\ -\cos\theta\tan\varphi_1 - \sin\theta\tan\varphi_2 & \sin\theta\tan\varphi_1 - \cos\theta\tan\varphi_2 & 1 \end{bmatrix} \begin{bmatrix} r_x \\ r_y \\ r_z \end{bmatrix} \quad (17)$$

4.2 Integrated stage control

The stage control can be separated into two parts: the *xy*-plane position control and the *z*-height control. For the *x*- and *y*- axis, we used a double-loop control structure (see Fig. 5), where the stepper-motor is in charge of large displacements, while the PZT stage makes precision movements. That is, the stepper-motor errors, $e_S^x = x_S - r_x^*$ and $e_S^y = y_S - r_y^*$, are fed back to control the stepper motor stage. On the other hand, the integrated errors, $e_x = x_S + x_P - r_x^*$ and $e_y = y_S + y_P - r_y^*$, are used to regulate the PZT stage. However, the PZT displacements are limited, and will be saturated if the commands (r_x^* or r_y^*) are larger than 6μm. Therefore, we designed the following anti-locking function:

$$e_P^i = \begin{cases} e_i, \text{ if } |e_i| \le 6(\mu\text{m}),\ i = x \text{ or } y \\ 0, \text{ otherwise} \end{cases} \quad (18)$$

which limits the PZTs to correct displacement errors (e_P^x and e_P^y) within ±6μm.

We observed that the required travel for the z-axis was about 15μm to adjust the tilting effects for a travel of 500μm with a tilting angle of 1.72o. Therefore, we used a PZT alone to handle the displacement requirement, by feeding back the PZT error for closed-loop control. In the future, we will integrate a z-axis stepper-motor stage to fabricate larger micro-structures.

We integrated the combined stage to track step commands. The experimental results are shown in Fig. 7(a), with a settling time of 107ms and a root-mean-square error (RMSE) of 74nm. The RMSE is large because the step motor chattered due to its resolution of 0.1μm. The chattering can be effectively reduced by a "hold-on mechanism" that turns off the step motors if both commands (r_x^* and r_y^*) and outputs (x_S and y_S) remain unchanged for forty steps. The modified responses are shown in Fig. 7(b), where the chattering is effectively reduced and the RMSE is reduced to 2.1nm.

We applied the combined stage to track step commands of 0.1, 1, 10, and 100 mm on the x- and y-axis. The experimental results are illustrated in Table 2, where the combined stage can keep constant accuracy, with RMSEs of less than 5.2 nm.

Table 2 Performance tests of the combined stage

Command	axis	100μm	1000μm	10mm	100mm
RMSE	x-	4.77	4.89	5.04	5.12
(nm)	y-	4.63	4.82	4.99	5.07
Settling	x-	0.16	0.22	1.23	12.15
time(s)	y-	0.15	0.22	1.21	12.14

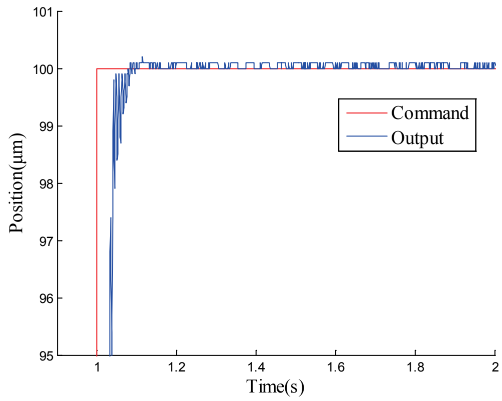

(a) Without mechanism

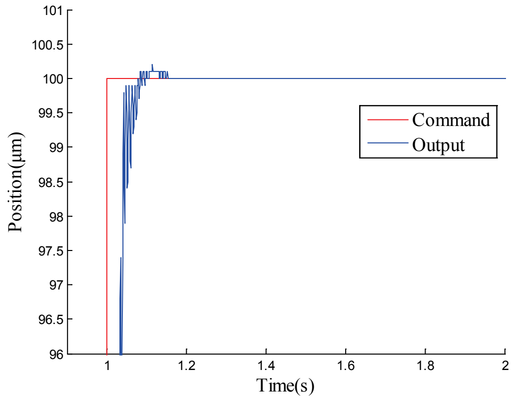

(b) With mechanism

Fig. 7 The effects of the hold-on mechanism.

5. TPP experiment and result

The schematic diagram of TPP micro fabrication system is shown in Fig. 8(a), where the laser power is controlled by the acouto-optic modulator while the laser beam sizes and parallels are adjusted by the beam expander. Furthermore, the Dichroic mirror reflects the laser with specific wavelength, while the objective lens focus the laser beams into the resin. We can control the resin position by the stage, and observe the process through the CMOS camera. The integrated system is shown in Fig. 8(b). An inverted OLYMPUS IX51 microscope is adopted to provide a solid frame for mounting the laser module and the objective lens. The magnification of the objective lens is 100 with a numerical aperture (NA) of 1.30. In addition, the applied polymer material is Ormocomp and the photoinitiator is 1,3,5-tris(2-(9-ethycabazyl-3)ethylene)benzene [11]. The specifications of the experiment setups are illustrated in Table 3. We switch on/off the laser by dividing the manufacturing paths into segments. For example, referring to Fig. 8(c), we make three vertical gratings by turning on the laser and moving the stage along segment 1, then switching off the laser during segment 2. Then we repeat the procedures in a similar way, i.e., switching on the laser during segments 3 and 5, and turning off it during segment 4. Note that the maximum speeds of the combined stage is about 8mm/s, which is the constrained by the maximum speed of the stepper motors. In the future, the travel speed might be increased by applying better stepper motors.

We next applied the integrated stage to fabricate micro-structures by TPP, as shown in Fig. 8(b). The microscope was connected to the laser source to trigger the TPP reaction. During TPP fabrication, the laser was fixed while the stage carried the resin (materials) to make movements. Therefore, the stage displacement commands should be opposite to the fabrication commands. We made words, gratings, and a micro Fresnel zone plate lens, and examined the experimental results by viewing scanning electronic microscope (SEM) images. We also defined performance indexes by the SEM image errors and optical properties, to compare the quality of the micro-structures. Based on the comparison, we further adjusted the controllers to improve system performance, and conducted experiments for verification.

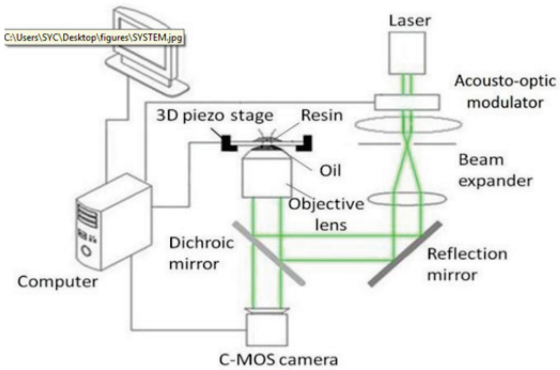

(a) Schematic diagram of the TPP system [11]

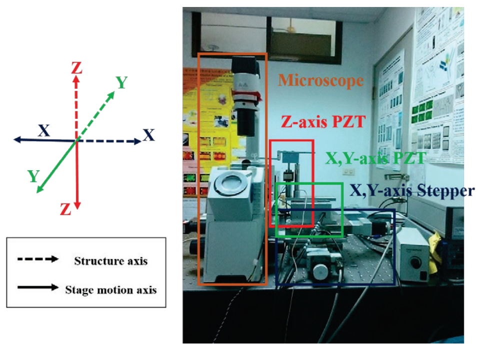

(b) The integrated hardware system

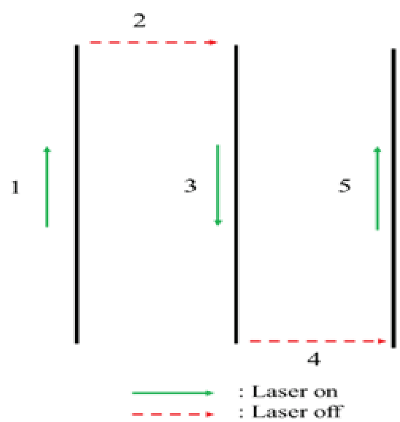

(c) The strategy of switching laser

Fig. 8 Integration with the TPP system.

Table 3 Specifications of laser module

Laser module	
Laser	Nd:YAG picosecond
wave length	532 nm
Repetition rate	130 kHz
Input laser power	26 mW
Peak power	200 W
Pulse energy	200 nJ
Acousto-optic modulation	AA Opto Electric MT200
Pulse width	550 ps
Material	
Resin	Ormocomp
Initiator	1,3,5-tris(2-(9-ethycabazyl-3)ethylene)benzene
Optics	
Objective lens	OLYMPUS UPlanFL N
Magnification	100x
Numerical aperture (NA)	1.30

5.1 Word plotting

First, we plotted the words "thank you" to verify the rotation matrix, because of their directional structures. We set $\theta = 0, \ \pm 30°$ for verification. Because the movements were about 100μm, the tilting effects were negligible; i.e., $\varphi_1 = \varphi_2 = 0$. Therefore, we applied the coordinate transformation matrix (13) to shape the commands, as illustrated in Fig. 9(a–b). The SEM images are illustrated in Fig. 9(c–e). From the results, the coordinate transformation and the command-shaping method are deemed effective in fabrication.

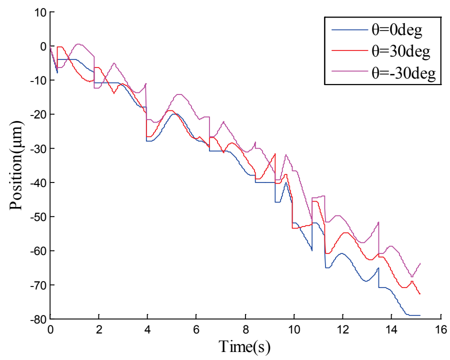

(a) x-axis commands

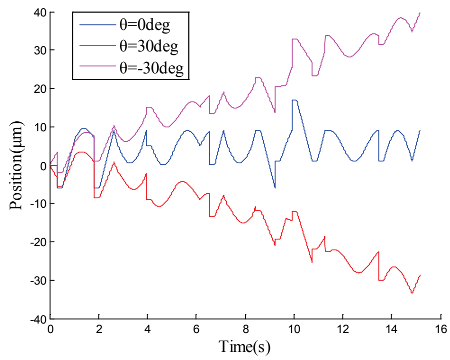

(b) y-axis commands

(c) SEM image with $\theta = 0^{\circ}$

(d) SEM image with $\theta = 30^{\circ}$

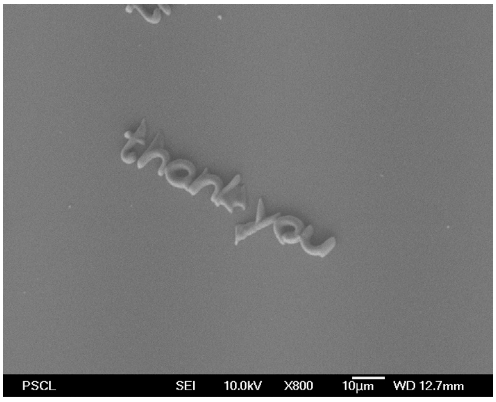

(e) SEM image with $\theta = -30^{\circ}$

Fig. 9 Word plotting.

5.2 Linear grating and image error

We then applied the integrated system to fabricate a $100\mu m \times 100\mu m$ linear grating with a pitch of 10μm. We performed a test run for calibration before fabrication, and calculated $\theta = 1.03^{\circ}$, $\varphi_1 = 0.57^{\circ}$, and $\varphi_2 = 0.69^{\circ}$. First, Fig. 10(a–b) shows the commands after coordinate transformation, which comprised steps and ramps. Second, we applied the controllers designed in Section 3 to fabricate the micro-structures, and then coated them for SEM scanning, as shown in Fig. 10(c). Third, we binarized the image by comparing it with a threshold, as illustrated in Fig. 10(d). Last, we constructed an ideal image model based on the scale of the SEM scan and the fabricated voxel width [11] (see Fig. 10(e)), and defined the image percentage error $e_i\%$ as follows:

$$\text{image percentage error}: \ e_i\% \equiv \frac{\text{error pixels}}{\text{ideal model pixels}} = \frac{\int_{x_0}^{x_e}\int_{y_0}^{y_e} e(x,y)dydx}{l_m \times w_m} \times 100\% \tag{19}$$

where (x_0, y_0) is the starting point and (x_e, y_e) is the end point (see Fig. 10(f)). l_m and w_m are the ideal length and width. For example, the micro grating of Fig. 10 has an image percentage error $e_i\% = 15.6\%$. In addition, we note that some gratings in Fig. 10(c) and (d) do not connect well. It is because the laser module cannot synchronize with the stage movements, i.e., the laser might be incorrectly switched on/off along the pre-set paths, and causes the disconnection. In the future, we aim to solve this problem by synchronously controlling the laser module and the combined stage.

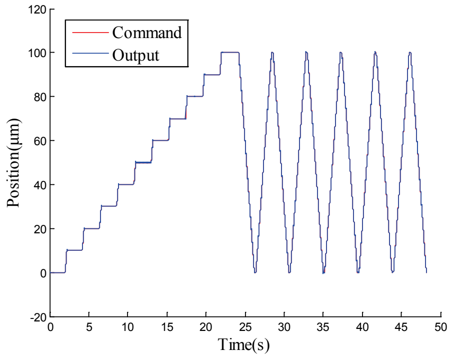

(a) x-axis commands

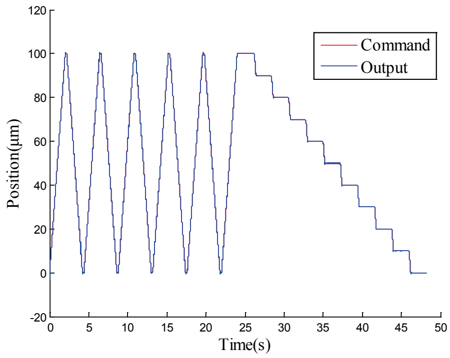

(b) y-axis commands

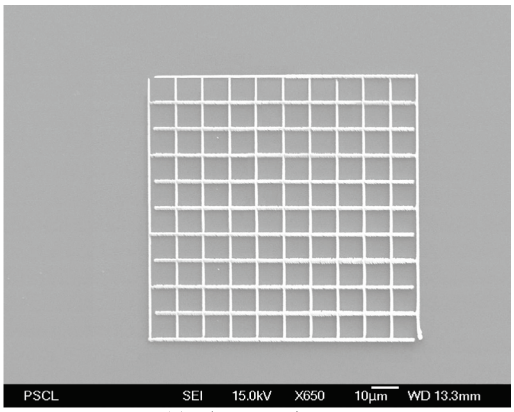

(c) The SEM image

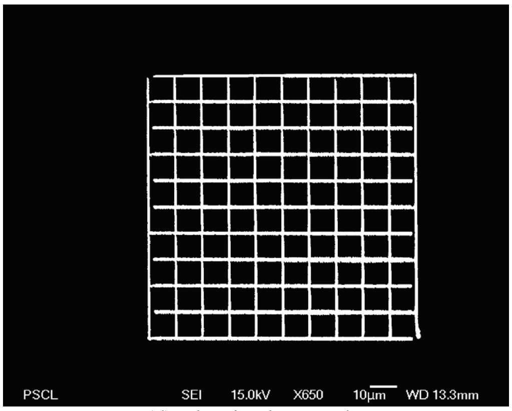

(d) Binarization results

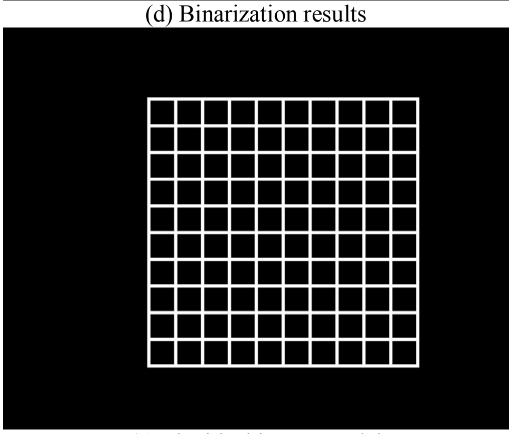

(e) The ideal image model

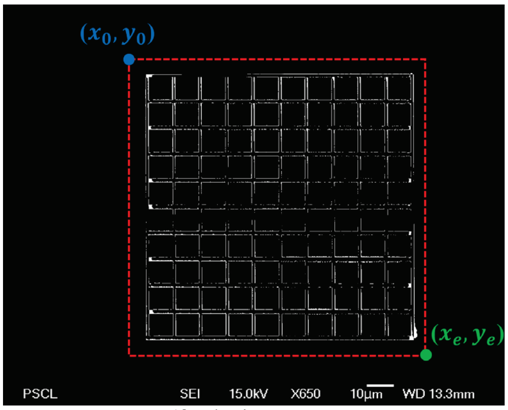

(f) The image error

Fig. 10 Linear gratings and performance analyses.

We further discuss the impacts of controller design on the image properties by designing several controllers to fabricate the linear gratings. Table 4 illustrates the tuned weighting functions for each controller. The controllers can be directly obtained by the methods of Section 3. We note that $e_i\%$ is related with the settling time of the PZT stage and the phase lag of the stepper-motor stage. For example, we compared (iii) and (iv) and found that $e_i\%$ is improved from 15.6% to 8.2% when the phase lag of the stepper-motor stage was reduced from 9.7 $^{\text{o}}$ to 3.6 $^{\text{o}}$. It is because the phase-lag degrades tracking ability and causes greater image errors. On the other hand, $e_i\%$ is improved from (ii) 17.2% to (iii) 15.6% when the settling time of the PZT

Table 4 Comparison of controllers for linear gratings

No.		PZT		Stepper-motor		Image error $e_i\%$
		Weighting	Settling-time	Weighting	Phase lag	
(i)	x	$W_P^x = \dfrac{6.5\times10^6}{s(s+300)^2}$	93ms	$W_S = \dfrac{200(s+2\pi\times50)}{(s+2\pi\times100)}$	17.6°	21.3%
	y	$W_P^y = \dfrac{5\times10^6}{s(s+300)^2}$	96ms	$W_S = \dfrac{200(s+2\pi\times50)}{(s+2\pi\times100)}$	17.6°	
(ii)	x	$W_P^x = \dfrac{6.5\times10^6}{s(s+300)^2}$	93ms	$W_S = \dfrac{300(s+2\pi\times60)}{(s+2\pi\times100)}$	9.7°	17.2%
	y	$W_P^y = \dfrac{5\times10^6}{s(s+300)^2}$	96ms	$W_S = \dfrac{300(s+2\pi\times60)}{(s+2\pi\times100)}$	9.7°	
(iii)	x	$W_P^x = \dfrac{572(s+2\pi\times50)}{s(s+2\pi\times60)}$	60ms	$W_S = \dfrac{300(s+2\pi\times60)}{(s+2\pi\times100)}$	9.7°	15.6%
	y	$W_P^y = \dfrac{600(s+2\pi\times50)}{s(s+2\pi\times60)}$	58ms	$W_S = \dfrac{300(s+2\pi\times60)}{(s+2\pi\times100)}$	9.7°	
(iv)	x	$W_P^x = \dfrac{572(s+2\pi\times50)}{s(s+2\pi\times60)}$	60ms	$W_S = \dfrac{600(s+2\pi\times50)}{(s+2\pi\times60)}$	3.6°	8.2%
	y	$W_P^y = \dfrac{600(s+2\pi\times50)}{s(s+2\pi\times60)}$	58ms	$W_S = \dfrac{600(s+2\pi\times50)}{(s+2\pi\times60)}$	3.6°	
(v)	x	$W_P^x = \dfrac{180}{s}$	11ms	$W_S = \dfrac{600(s+2\pi\times50)}{(s+2\pi\times60)}$	3.6°	7.8%
	y	$W_P^y = \dfrac{377}{s}$	9ms	$W_S = \dfrac{600(s+2\pi\times50)}{(s+2\pi\times60)}$	3.6°	

stage decreases from 93ms to 60ms. The reason is that the PZT with smaller settling time can compensate small tracking errors (with 5um) faster to reduce the image error $e_i\%$.

Based on these criteria, we further modified the weighting functions and iteratively checked the settling time and phase lag, and selected the following weightings:

$$W_P^x = \frac{180}{s}, W_P^y = \frac{377}{s}, W_S = \frac{600(\mathrm{s}+2\pi\times 50)}{(\mathrm{s}+2\pi\times 60)} \qquad (20)$$

and designed the following controllers:

$$K_\infty^x = \frac{2.094s^4 + 1.027\times 10^4 s^3 + 7.470\times 10^7 s^2 + 6.311\times 10^{10} s + 1.847\times 10^{13}}{s^4 + 2.496\times 10^4 s^3 + 3.201\times 10^7 s^2 + 9.415\times 10^{10} s + 3.755\times 10^{13}},$$
$$K_\infty^y = \frac{0.8738s^4 + 7078s^3 + 2.399\times 10^8 s^2 + 1.265\times 10^{11} s + 2.800\times 10^{15}}{s^4 + 1.247\times 10^4 s^3 + 3.081\times 10^8 s^2 + 7.948\times 10^{11} s + 2.329\times 10^{15}}, \qquad (21)$$
$$K_\infty^S = \frac{0.9796s + 368.2}{s + 360.7},$$

which gave settling time of 11ms and 9ms for the *x*- and *y*-axis, respectively, and the phase lag of 2.1° for the stepper-motor stage. As a result, the percentage error $e_i\%$ is further improved to $e_i\% = 7.5\%$. The hardware constraints create difficulties in achieving further reductions in the system settling time and phase lags. Nevertheless, we can consider other TPP techniques; e.g., turning off the laser during overshoots to avoid undesired polymerization [11][24]. The image percentage error can be further improved to $e_i\% = 5.5\%$.

5.3 Fresnel zone plate and imaging quality

Last, we applied the integrated system to fabricate a micro Fresnel zone plate (FZP) lens. The FZP was designed with an ideal focal length of 500µm, for light with a wavelength of 632.8nm. Similarly, we found the rotation and tilting angles by pre-experimental tests, and obtain $\theta = 0.92^{\circ}$, $\varphi_1 = \text{-}0.69^{\circ}$, and $\varphi_2 = 0.74^{\circ}$ for coordinate transformation. The position commands r_x^*, r_y^*, r_z^* are shown in Fig. 11(a–c), which comprises sinusoidal signals. Fig. 11(d) shows a result for an SEM image. We further defined the following performance indexes to quantify the optical quality of the micro-lens:

(1) *focal percentage error* $e_f\%$: we compared the ideal focal length f_{ideal} [25] with the measured focal distance f_{measured} [26][27], and defined:

$$e_f\% = \frac{f_{\text{ideal}} - f_{\text{measured}}}{f_{\text{ideal}}} \times 100\% \qquad (22)$$

(2) *light intensity* and *sharpness*: the light intensity and sharpness of the CMOS images obtained with five different lenses, which were fabricated using the five designed controllers illustrated in Table 3, are shown in Fig. 12(a), where the image intensity and sharpness can also be used to represent the quality of the micro-lens as shown in Fig. 12(b) and (c).

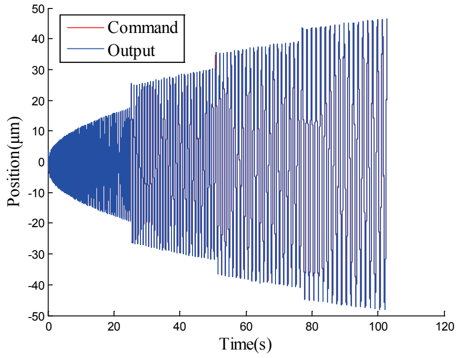

(a) *x*-axis displacements

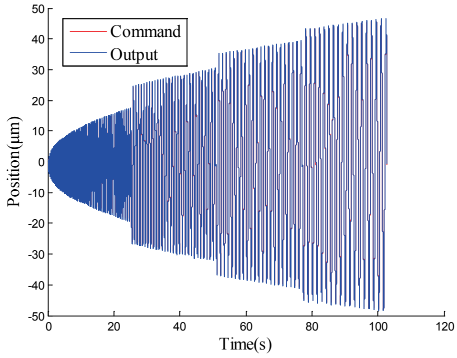

(b) *y*-axis displacements

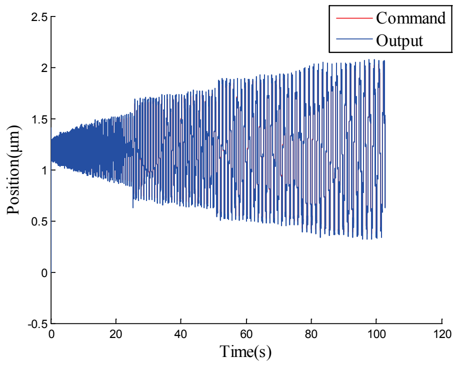

(c) *z*-axis displacements

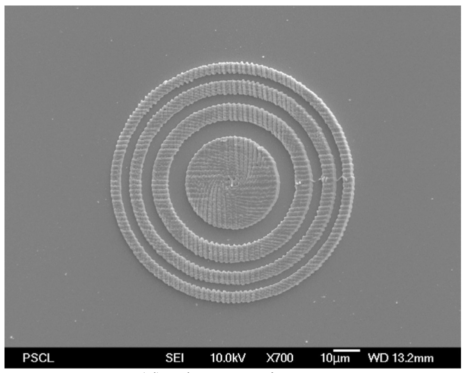

(d) The SEM image

Fig. 11 Fabrication of the micro FZP lens.

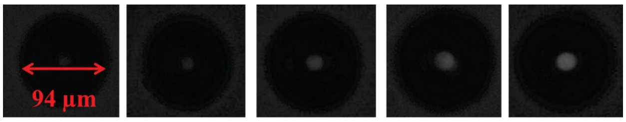

(i) (ii) (iii) (iv) (v)

(a) FZP samples

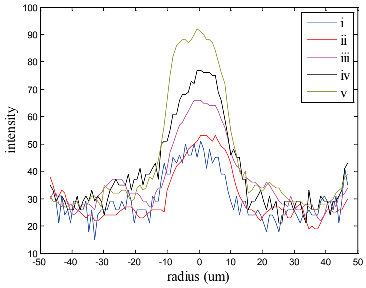

(b) Intensity

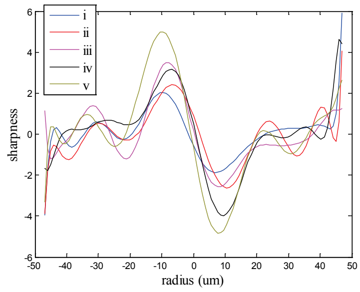

(c) Sharpness

Fig. 12 Imaging quality analyses.

We implemented the controllers designed in Section 3 to fabricate the FZP, which gave the focal percentage error $e_f\%$ =-2.6%, with an intensity of 66 and a sharpness of 3.103. We further applied the controllers of Table 4 to discuss the relationship between controllers and lens quality. The results are illustrated in Table 5, where we found that the performance indexes are related with the stage bandwidth, because a system's bandwidth represents its speed to track commands [28]. The manufacturing commands are designed for ideal FZP with specific focal lengths. Therefore, when the bandwidth is decreased, the ability to dynamically track these commands is reduced so that the fabricated FZP has larger focal errors. For example, comparing controllers (ii)(iii), $e_f\%$ was improved from -3.0% to -2.6% and the intensity/sharpness were improved from 53/2.715 to 66/3.103 by increasing the bandwidth of the PZT stage from 22Hz to 64Hz. On the other hand, comparing controllers (iii) and (iv) show that $e_f\%$ was improved from -2.6% to -2.0% and the intensity/sharpness were improved from 66/3.103 to 78/4.327 by increasing the bandwidth of the stepper-motor stage from 4Hz to 8Hz. Last, controller (v) gave the best performance by increasing the bandwidths of both stages.

Furthermore, the diffraction efficiency of the FZP can also be used to measure the fabrication performance. The diffraction efficiency is defined as [29]:

Table 5 Comparison of controllers for the micro FZP lens.

No.		PZT Weighting	PZT BW	Stepper-motor Weighting	Stepper-motor BW	Focal error $e_f\%$ / Intensity/Sharpness
(i)	x	$W_P^x = \dfrac{6.5\times10^6}{s(s+300)^2}$	22Hz	$W_S = \dfrac{200(s+2\pi\times50)}{(s+2\pi\times100)}$	2Hz	-3.2%
	y	$W_P^y = \dfrac{5\times10^6}{s(s+300)^2}$	20Hz	$W_S = \dfrac{200(s+2\pi\times50)}{(s+2\pi\times100)}$	2Hz	51/2.252
(ii)	x	$W_P^x = \dfrac{6.5\times10^6}{s(s+300)^2}$	22Hz	$W_S = \dfrac{300(s+2\pi\times60)}{(s+2\pi\times100)}$	4Hz	-3.0%
	y	$W_P^y = \dfrac{5\times10^6}{s(s+300)^2}$	20Hz	$W_S = \dfrac{300(s+2\pi\times60)}{(s+2\pi\times100)}$	4Hz	53/2.715
(iii)	x	$W_P^x = \dfrac{572(s+2\pi\times50)}{s(s+2\pi\times60)}$	64Hz	$W_S = \dfrac{300(s+2\pi\times60)}{(s+2\pi\times100)}$	4Hz	-2.6%
	y	$W_P^y = \dfrac{600(s+2\pi\times50)}{s(s+2\pi\times60)}$	63Hz	$W_S = \dfrac{300(s+2\pi\times60)}{(s+2\pi\times100)}$	4Hz	66/3.103
(iv)	x	$W_P^x = \dfrac{572(s+2\pi\times50)}{s(s+2\pi\times60)}$	64Hz	$W_S = \dfrac{600(s+2\pi\times50)}{(s+2\pi\times60)}$	8Hz	-2.0%
	y	$W_P^y = \dfrac{600(s+2\pi\times50)}{s(s+2\pi\times60)}$	63Hz	$W_S = \dfrac{600(s+2\pi\times50)}{(s+2\pi\times60)}$	8Hz	78/4.327
(v)	x	$W_P^x = \dfrac{180}{s}$	105Hz	$W_S = \dfrac{600(s+2\pi\times50)}{(s+2\pi\times60)}$	8Hz	-1.6%
	y	$W_P^y = \dfrac{377}{s}$	108Hz	$W_S = \dfrac{600(s+2\pi\times50)}{(s+2\pi\times60)}$	8Hz	93/5.722

$$\eta = \frac{P_{diff}}{P_{inc}} \qquad (23)$$

where P_{diff} and P_{inc} represent the power of the diffracted light beam and the incident power of the beam. We can use the intensity data of Fig. 12(b) and calculate the diffraction efficiencies as (i) 53.15 % (ii) 51.48 % (iii) 54.77 % (iv) 62.05% (v) 64.79 %, which are basically consistent with the intensity and sharpness analyses shown in Table 5. The only exception is sample (i) and (ii), where the intensity/sharpness are increased but the efficiency is decreased. It is because their intensity is not obviously different (see Fig. 12 (b)).

6. Conclusion

This paper has applied a combined stage to micro fabrication. The stage consisted of a PZT stage and a stepper-motor stage to achieve long-stroke and high precision positioning. The combined stage was then integrated with a TPP system to fabricate micro-structures. First, we identified the stage models and designed robust loop-shaping controllers for both stages. Second, we assembled these two stages and designed a control structure to achieve a RMSE of 2.1nm with a long stroke of 10cm. We also proposed coordinate transformation to compensate for stage rotation and tilts. Third, we integrated the combined stage with the TPP system and fabricated micro-structures, including words, gratings, and an FZP lens. Last, we proposed performance indexes to quantify the micro-fabrication qualities by image processing and optical analysis. We can use these results for further adjustment of the control design to improve the qualities of TPP fabrication. In addition, the current combined stage can travel up-to 10cm with RMSEs of less than 5.2nm, but the sizes of microstructures are still limited because the resin deteriorates when the manufacturing time increases, and the z-axis PZT can only adjust titling within small travels. In the future, we will adjust the resin recipe to allow more manufacturing time, and to integrate a z-axis stepper-motor to compensate tilting effects for manufacturing large microstructures.

Acknowledgment

This work was financially supported in part by the Ministry of Science and Technology of Taiwan under Grands 98-2221-E-002-167-MY3 and 102-2221-E-002-198. The authors would also like to thank Prof. Jia-Han Li for his advice in revising the paper.

References

[1] Q. Xu: IEEE Trans. Control Syst. Technol., 23, (2014) 297.
[2] J.Y. Peng, and X.B. Chen: IEEE/ASME Trans. Mechatron., 19, (2012) 88.
[3] B.J. Kenton, and K. K. Leang: IEEE/ASME Trans. Mechatron., 17, (2011) 356.
[4] J. Yi, S. Chang, and Y. Shen: IEEE/ASME Trans. Mechatron., 14, (2009) 456.
[5] L. Liu, K.K. Tan, C.S. Teo, and S.L. Chen: IEEE Trans. Control Syst. Technol., 21, (2012) 1834.
[6] R.C. Wu, I.H. Tsai, F.C. Wang, and J.Y. Yen: Proc. 2013 IEEE/SICE Int. Symp. System Integration, Kobe, (2013) p.138.
[7] J. Li, H. Zhao, X. Qu, H. Qu, X. Zhou, Z. Fan, Z. Ma, and H. Fu: Sens. and Actuators A: Phys., 222, (2015) 87.
[8] Y.Y. Chen, R.C. Wu, F.C. Wang, and J.Y. Yen: Proc. 2014 SICE SICE Annu. Conf., Sapporo, (2014) p.432.
[9] M. Göppert-Mayer: Annalen der Physik, 401, (1931) 273.
[10] W. Kaiser and C. Garrett: Phys. Rev. Lett., 7, (1961) 229.
[11] T.T. Chung, Y.T. Tu, Y.H. Hsueh, S.Y. Chen, and W.J. Li: Int. J. Autom. Smart Technol., 3, (2013) 131.
[12] C.L. Lin, Y.H. Lee, C.T. Lin, Y.J. Liu, J.L. Hwang, T.T. Chung, and P.L. Baldeck: Opt. Express, 19, (2011) 20604.
[13] J. Kumpfmueller, K. Stadlmann, V. Satzinger, Z. Li, J. Stampfl, and R. Liska: J. Laser Micro/Nanoengin., 6, (2011) 195.
[14] T. Stichel, B. Hecht, R. Houbertz, and G. Sextl: J. Laser Micro/Nanoengin., 5, (2010) 209.
[15] M.T. Do, T. T. N. Nguyen, Q. Li, H. Benisty, I. Ledoux-Rak and N. D. Lai: Opt. Express, 21, (2013) 20964.
[16] D. Wu, L.G. Niu, Q.D. Chen, R. Wang, and H.B. Sun: Optics Lett., 33, (2008) 2913.
[17] D. Wu, J. Xu, L.G. Niu, S.Z. Wu, K. Midorikawa, and K. Sugioka: Light Sci. Appl., 4, (2015) e228.
[18] P.V. Overschee, and B.D. Moor: Autom., 30, (1994) 75.
[19] K. Glover, and D. McFarlane: IEEE Trans. Autom. Control, 34, (1989) 821.
[20] J. Doyle, and B. Francis: Macmillan (1990).
[21] K. Zhou: Prentice Hall Int. (1998).
[22] D. McFarlane, and K. Glover: IEEE Trans. Autom. Control, 37, (1992) 759.
[23] F.C. Wang, L.S. Chen, Y.C. Tsai, C.H. Heish, and J.Y. Yen: J. Vib. Control, 20, (2014) 885.
[24] R. Guo, S. Xiao, X. Zhai, J. Li, A. Xia, and W. Huang: Opt. Express, 14, (2006) 810.
[25] L.G. Niu, D. Wang, T. Jiang, S.Z. Wu, A.W. Li, and J.F. Song: Opt. Commun., 284, (2011) 777.
[26] H.J. Tiziani, M. Wegner, and D. Steudle: Soc. Photo-Opt. Instrum. Eng., 39, (2000) 32.
[27] W. Moench, and H. Zappe: J. Opt. A., 6, (2004) 330.
[28] R.C. Dorf, and R.H. Bishop: “Morden Control System”, (Pearson, New Jersey, 2011) p.602.
[29] S. Tamura: “Multilayer Fresnel Zone Plate with High-Diffraction Efficiency: Application of Composite Layer ti X-ray Optics” ed. by J. Cuppoletti (InTech, 2011) p. 637.

(Received: October 7, 2015, Accepted: December 10, 2015)